www.ietdl.org

Published in IET Microwaves, Antennas & Propagation
Received on 20th December 2010
Revised on 13th May 2011
doi: 10.1049/iet-map.2010.0611

ISSN 1751-8725

In-silico hyperthermia performance of a near-field patch antenna at various positions on a human body model

S. Curto[1] *T.S.P. See*[2] *P. McEvoy*[1] *M.J. Ammann*[1] *Z.N. Chen*[2]

[1]*Antenna and High Frequency Research Centre, Dublin Institute of Technology, Dublin 8, Ireland*
[2]*RF & Optical Department, Institute for Infocomm Research, 1 Fusionopolis Way, #21-01 Connexis, South Tower, Singapore 138632, Singapore*
E-mail: max.ammann@dit.ie

Abstract: A compact patch applicator designed to enhance targeted energy coupling at 434 MHz is a key enabler for sensitising temperature increments in body regions containing superficial tumours. A detailed finite difference time domain (FDTD) body model is used to explore simulated radio-frequency (RF) coupling and temperature increments for typical clinical conditions. The antenna impedance matching, specific absorption rate and thermal distribution parameters are evaluated to identify applied performance outcomes. The analysis reveals physiological-RF coupling patterns for an optimised closely coupled single-element applicator.

1 Introduction

The effectiveness of radio-frequency (RF) hyperthermia treatment systems for oncology [1] or injured muscular tissue [2] is proportional to the transfer of electromagnetic energy into the targeted body region. Antenna applicators with RF sources of sufficient power are selected for an energy deployment rate to overcome cooling that vascular perfusion and perspiration contribute to natural thermal regulation. Single-element near-field antenna applicators are suited to lower-cost clinical systems for tissue treatment at superficial depths [3]. Applied clinical setup models require enhanced biological details over conventional homogeneous or planar-layered body models. The performance of the near-field-loaded antenna reported here is evaluated with a numerical human model for resonant frequency and impedance match insensitivity to dielectric load variations at different anatomy locations.

Positioning the antenna radiating near-field in close proximity to a patient increases the mutual interaction of the radiator and the body. However, precipitous sub-wavelength variations in near-fields produce irregular amplitude and phase patterns that add complexity to the analysis of the antenna coupling performance. Furthermore, the electric field components scatter among the arbitrary shapes and layers of differing tissues in the treatment area. The energy coupling is dependent on multiple factors, inter alia, the radiation pattern, variation of proximity from the tissue, varying waterbolus profile depths that conform to the body surface, diversity of anatomical shapes, electromagnetic responses in biological tissues and furthermore by individual physiological responses because of age, metabolic rates or a pathological stage.

A near-field hyperthermia antenna design should be capable of targeting energy without causing adverse power concentrations in the superficial tissue layers. Measurement of distributed thermal patterns in bulk tissue is difficult and design analysis is more expedient in silico provided the software model is a reasonably accurate representation of in vitro clinical conditions. One-dimensional [4], coarse-resolution homogeneous [5] and planar-layered [6] numerical human models can reveal a basic distribution of coupled energy. However, simplified models can compromise the clinical treatment setup and patient comfort by underestimating the actual peak specific absorption rate (SAR) and localised high-intensity patterns.

In order to assess a range of coupling variations for different body areas, the antenna was modelled at the rear of the head, between the shoulder blades (inter-scapular) and in front of the stomach (epigastrium). Surface-cooling waterboluses [7, 8] which conformed to the body shapes were included for improved representation of clinical treatment setups. Models reveal the energy distributions and their dependence on the geometric features of the applicator antenna. Furthermore, indicative body thermal responses to the applicator help to establish useful basis for pre-treatment planning [9]. The antenna design seeks to offer a stable coupling pattern for a range of anatomy features [10]. This permits technicians to apply treatment to various locations of a patient without having select alternate pre-optimised applicators.

2 Materials and methodology

2.1 Hyperthermia antenna design

Fig. 1 shows the compact 434 MHz printed patch antenna on a low-loss tangent, double-sided Taconic RF-35 dielectric

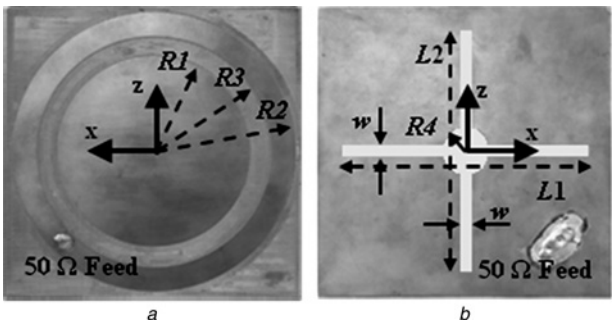

Fig. 1 *Fabricated antenna and dimensions*

a Front side (towards tissue)
b Rear side (away from tissue)
The dimensions are: $R1 = 42$ mm, $R2 = 51$ mm, $R3 = 62$ mm, $R4 = 10$ mm, $L1 = 106$ mm, $L2 = 108$ mm, $w = 4$ mm. The 50 Ω feed is in the concentric annular ring at coordinates $(x, z) = (40, -40)$ mm

substrate, $\varepsilon_r = 3.5$, $\tan\delta = 0.0018$. The slotted features are designed to minimise substrate dimensions to $130 \times 130 \times 3$ mm and to focus the radiated energy concentrically into the targeted tissue treatment zone. A description of the antenna design process and a comparison of the basic functionality with other applicator approaches are reported in [11].

2.2 Human body model

Extensive computational resources are necessary for the full-wave electromagnetic simulation of detailed anatomy models. Free-space wavelengths of 0.7 m far exceed the dimensions of the morphological features which range from 1×10^{-9} m for molecules, 1×10^{-7} m for cells and millimetre scales for tissues etc. Intricate elements like nerve fibres, blood vessels or muscle fibres are inherently anisotropic but such detail is discarded by classifying their enclosing tissues as homogeneous Debye materials. However, multi-tissue whole-body models provide an improved analysis baseline for complex electromagnetic coupling with arbitrary-shaped tissues [12, 13] and avoid simulation artefacts because of truncation of large organs and conductive tissues. The SAR and temperature profile estimates can enhance both the antenna design and clinical dosage planning [14].

The Remcom human body derived from the Visible Human Project data [15] was selected as the main heterogeneous model with the XFDTD electromagnetic solver [16]. The human model has a height of 1.8 m, a mass of 103 kg and comprises 23 tissue types with frequency-dependent electrical and thermal properties. The body model had a predefined 5 mm voxel resolution which was segmented from an adult male tomography of magnetic resonance images with 1 mm step cross-sections [15]. It was centre located in a grid with dimensions $0.77 \times 0.52 \times 2.08$ m with perfectly matched absorbing layers of seven cells deep with a minimum separation distance of 100 mm. The conductivity, density and relative permittivity values for the simulated body tissues are listed in Table 4 [17] and thermal properties are listed in Table 5 [16] (in the Appendix).

An adaptive mesh with a minimum cubic cell dimension of 1 mm ($\sim 1.4 \times 10^{-3} \times \lambda_0$) was defined for the antenna structure and the targeted body areas. The mesh resolutions were a trade between available computational resources and inaccuracies because of electric field or surface current orientation alignments with under-resolved geometric features. The simulation boundary conditions were perfectly matched absorbing layer of seven cells deep. More than 20 million cells were generated, which required 1.03 Gbytes of memory and typically 10 h on a 3.4 GHz PC with 4 Gbytes of RAM.

2.3 Antenna body positions

The conductivity-to-density ratio column in Table 4 indicates absorption rates of the tissue types. Although fat absorbs only 6% that of muscle, the antenna-body coupling is also influenced by proximity, aperture loading of tissue volumes, contoured tissue layering and organ shapes. A range of coupling performance was assessed at three locations shown in Fig. 2. The antenna was oriented perpendicular to the sagittal plane and parallel with and centred on the coronal plane.

The tissue compositions and shapes differ at each position, as detailed in Fig. 3. The head area model comprised a 5 mm layer of skin over a layer of yellow marrow which contains cortical and cancellous bone structures with cerebrospinal fluid involving grey and white matter. The model of the inter-scapular area of the back consisted of 10 mm-thick skin layer next to a variable layer of fat tissue and muscle. The cortical bone and white matter cover the spine, which was modelled as cancellous bone, cartilage and nerves.

The epigastrium model had a skin layer with a very thick sub-layer of fat (around 100 mm) which contains muscle, small intestine, pancreas and the stomach. Although the tissue layer thicknesses and shapes are distorted following the MRI, segmentation and voxel sampling, the multi-tissue features are an improved portrayal compared to homogeneous and planar layer models.

When the antenna is positioned at the head, it can be used to treat various types of brain or meninges cancers. Melanoma, vertebral or sarcoma cancers can be targeted from the inter-scapular position and superficial adenocarcinoma can be treated from the epigastrium.

Clinical applications employ waterboluses to cool the irradiated surface skin area and to improve the coupling.

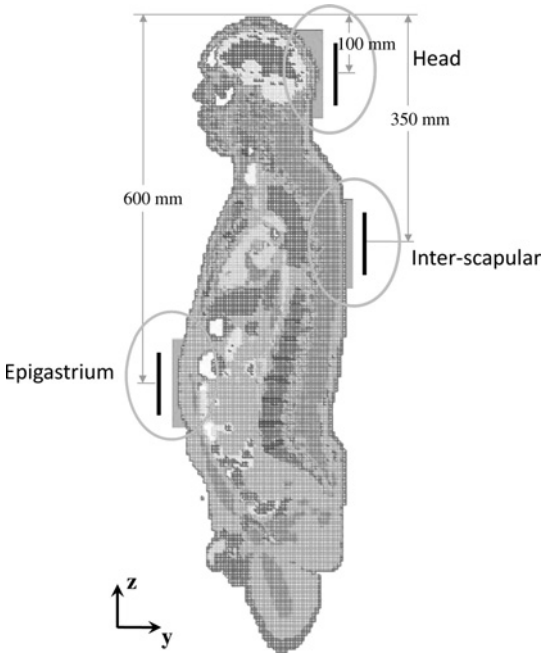

Fig. 2 *Sagittal plane section of human body model and antenna positions*

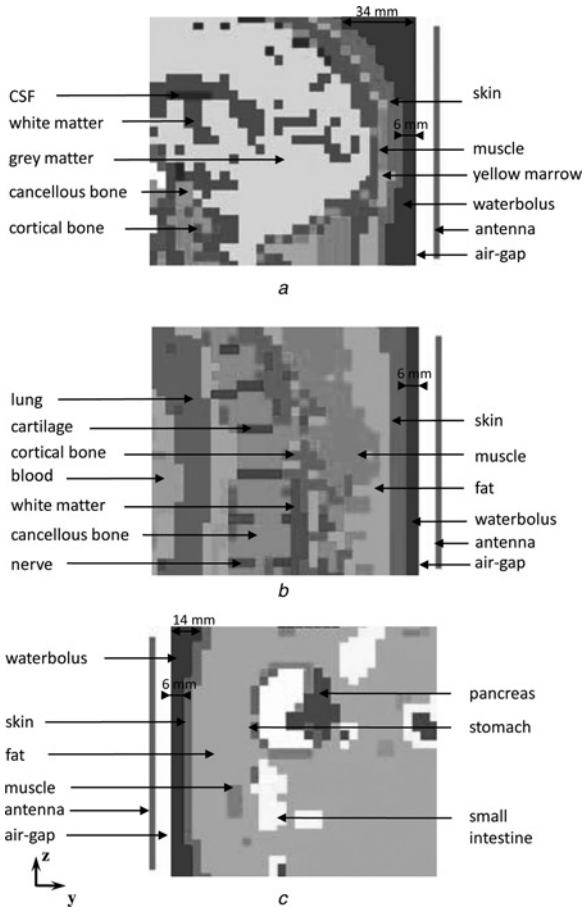

Fig. 3 *Tissue structures*

a Head
b Inter-scapular
c Epigastrium areas

Unlike previous studies of frequency-dependent surface wave oscillations with planar body models [7, 8] the waterbolus profile depths conformed to body's curved areas. The de-ionised water had permittivity $\varepsilon_r = 76$, conductivity $\sigma = 0.001$ S/m and covered a 200×200 mm area. The waterbolus thickness from the antenna centre to the edge ranged from 6 to 34 mm. The antenna was positioned close to the skin to minimise power loss in the bolus [10] but with a gap to minimise sensitivity to variations between patients. Approximately 22.4, 100 and 41.4% of the antenna radiating surface was loaded by the close proximity of the body features at the respective head, inter-scapular and epigastrium positions.

2.4 SAR and temperature analysis

SAR patterns were normalised to the antenna input power of 1 W and evaluated for 1 g averaged spatial peak SAR to mitigate against multi-tissue averaging across tissue boundaries [18, 19]. Iso-line plots for 50, 25% and $1/e^2$ SAR penetration depths were selected for consistency with methods employed in [20, 21] and European Society for Hyperthermic Oncology guidelines for homogeneous or layered body models.

Although temperature increments to 45°C and above are reported as hyperthermia treatment objectives, the doses can be referenced to cumulative equivalent minutes for a 43°C threshold [22]. The aim is to enhance the effectiveness of the radiotherapy with a RF power level setting that avoids thermal tolerance during follow up clinical treatment sessions [23]. The Pennes bio-heat equation [24] was used to calculate the temperature increments in a 23°C background within the Remcom application.

3 Methodology

The waterbolus thickness and the waterbolous–antenna air-gap dimensions were optimised for $|S_{11}|$ and peak SAR using the heterogeneous body model at the three sample treatment positions.

A comparison of body models was made to quantify the effects that body shapes and tissue layers have on the predicted coupling with the antenna. The comparison models were a planar-layered model (comprising skin, fat and muscle) and a homogeneous body model (same body shape than the heterogeneous model, but with all the tissues with properties of muscle tissue).

The temperature distribution analysis uses the heterogeneous body model but the calculation does not account for natural physiological responses to temperature rises and probably underestimates the dynamics of the natural cooling processes [14]. Accordingly, the static perfusion rates of the tissues were doubled from the base values to quantify additional antenna input powers at the three body treatment positions.

Additionally, the simulation technique was corroborated by measurements of the DASY4 SAR setup with a homogenous lossy liquid phantom.

4 Results

4.1 Waterbolus effects

Waterboluses with thicknesses 6, 8 and 10 mm along the centre of the antenna radiating axis were evaluated for optimum $|S_{11}|$ and peak SAR performance with the heterogeneous body model. The various dimensions were assessed with a range of antenna–waterbolus air-gaps between 2 and 16 mm in 2 mm steps. Thinner waterbolus dimensions were discounted for limited cooling capability and waterboluses in the $5 - 10$ mm range produced more even SAR distributions [7, 8]. Fig. 4*a* shows that increasing the waterbolus thickness with a fixed 10 mm air-gap impaired the impedance matching but did not affect the SAR significantly. Fig. 4*b* illustrates that air-gap increment from 2 to 12 mm for a 6-mm thick waterbolus improves the impedance matching but extended air-gap dimensions degrade the matching. The peak SAR reduces as the air-gap increases because of the bigger antenna–tissue separation. A 6-mm-thick waterbolus with a 10-mm air-gap produces the highest peak SAR with a corresponding $|S_{11}|$ of around -8 dB at 434 MHz. This setup configuration is used in the clinical modelling of the following results.

4.2 In-silico specific absorption rate

Initial analysis using a planar tri-layered tissue model and a homogeneous (muscle equivalent) body model explored influences of tissue loading and anatomical shapes on the power deposition mechanism. A 200×200 mm planar model comprised layers of skin (5 mm), fat (20 mm) and muscle (75 mm) for comparison with the heterogeneous epigastrium features. The results are shown in Table 1.

Figs. 5*a*–*c* show the SAR patterns in the sagittal plane for the homogeneous muscle model at the head, inter-scapular

doi: 10.1049/iet-map.2010.0611

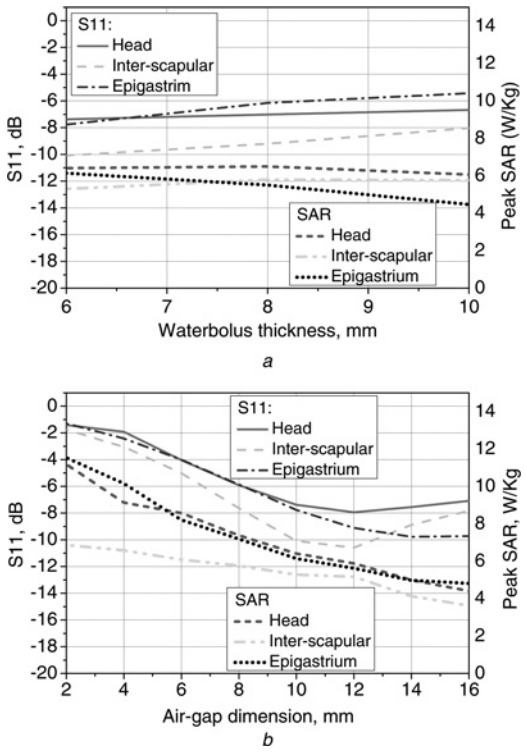

Fig. 4 *|S11| and peak SAR at 434 MHz*

a Waterbolus thicknesses with 10 mm air-gap dimension
b Air-gap dimensions with 6 mm waterbolus thickness for the heterogeneous body model

Table 1 Planar-layered and homogeneous models: peak SAR values and penetration depths

Model area	Peak SAR, W/kg	50% SAR, mm	25% SAR, mm	$1/e^2$ SAR, mm
planar layered	5.54	7	9	51
head	4.20	22	37	53
inter-scapular	3.75	32	49	60
epigastrium	3.95	25	47	56

and epigastrium positions. The peak SAR is aligned with the antenna radiating centre axis and the smooth distributions were only distorted at the epigastrium because of discontinuities at the air-filled cavities in the stomach and small intestine. Table 1 summarises the SAR and penetration depths for the planar-layered and homogeneous muscle body models. Figs. 5*d*–*f* show the sagittal plane SAR patterns for the heterogeneous model at the head, inter-scapular and epigastrium positions. The peak SAR is 6 ± 1 mm below the surface and is aligned with the feed diagonal and the antenna centre. By inspection, the 50% iso-SAR corresponds with the skin–fat interface and there are less absorbing sub-layers because of yellow marrow at the head and fat tissue at the inter-scapular and epigastrium positions. Secondary higher absorption zones occur below the yellow marrow and fat layers, which correspond with the antenna centre and occur in tissues with higher conductivity-to-density ratio, in particular, grey matter in the head, muscle in the inter-scapular position and the small intestine in the epigastrium. Table 2 summarises the SAR and penetration depths for the heterogeneous model.

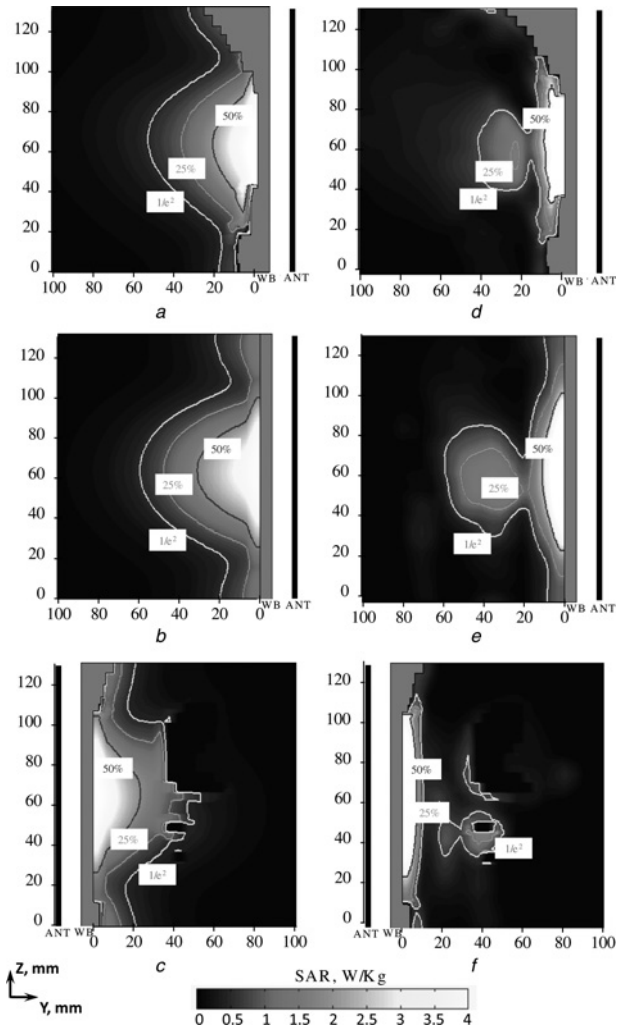

Fig. 5 *SAR patterns in the sagittal plane for the homogeneous (muscle) and heterogeneous body models*

a and *d* Head
b and *e* Inter-scapular
c and *f* Epigastrium positions

Table 2 Heterogeneous body model peak SAR values and penetration depths

Model area	Peak SAR, W/kg	50% SAR, mm	25% SAR, mm	$1/e^2$ SAR, mm	Secondary 25% SAR, mm
head	6.41	10	15	44	28
inter-scapular	5.28	10	17	60	52
epigastrium	6.14	7	9	55	51

4.3 *In-silico temperature*

The temperature response to energy deposition at the various body positions along the central sagittal plane of the heterogeneous body model is shown in Fig. 6. The waterbolus cooled the surface temperature to an approximate 5 mm depth. The 6°C rise to the target temperature of 43°C required an input power to the model positions of 75 W at the head, 92 W at the inter-scapular and 78 W at the epigastrium. Although the SAR peaks dominated near the surface, the energy penetration profile and the tissue

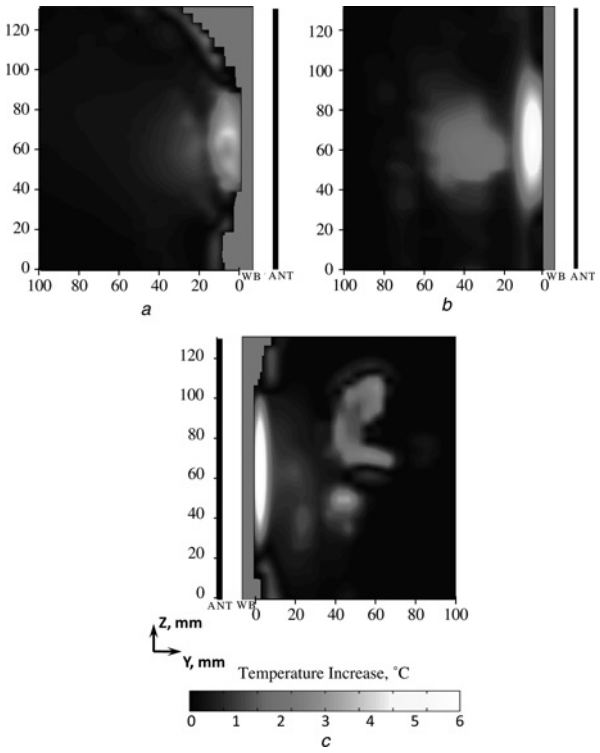

Fig. 6 *Sagittal plane temperature distributions*

a Head
b Inter-scapular
c Epigastrium positions with applied powers of 75, 92 and 78 W, respectively, for the heterogeneous body model

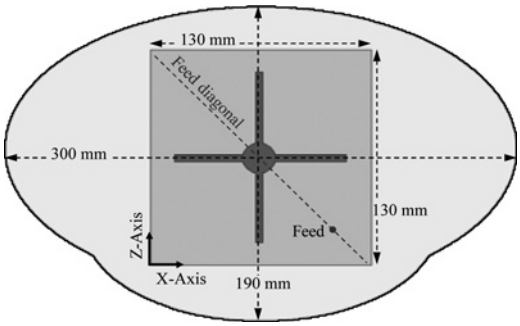

Fig. 7 *Antenna position at the base of the DASY phantom*

electrical and thermal properties combine to influence the resultant thermal changes. The strong perfusion rate in the head has limited the peak temperature to only just reaching 43°C. The maximum temperature rise in the inter-scapular position occurs at a shallower depth as compared to the peak SAR penetration. A secondary peak in the temperature rise corresponds with the $1/e^2$ iso-SAR contour. The peak temperature increments in the epigastrium occur mainly in the small intestine and stomach cavities.

The doubled perfusion rates required additional input powers of 4 W (79 W) at the head, 7 W (99 W) at the inter-scapular location and 3 W (81 W) at the epigastrium to reach the target temperature of 43°C.

4.4 Model validation

A comparison SAR measurement of a tissue-equivalent lossy liquid, using a SPEAG Dosimetric Assessment System [25], was used to corroborate the simulation approach. The robotic controlled precision probe was scanned in the *X*- and *Z*-axis with 1 mm step resolution and at a 4 mm distance from the inner surface of the 2-mm thick fibreglass phantom shell ($\epsilon_r = 3.7$). The parameters of the water–sugar-based homogeneous liquid phantom were measured as dielectric constant $\epsilon_r = 45.07$, conductivity $\sigma = 0.82$ S/m and density $\rho = 1250$ kg/m^3 at 434 MHz. Following a system calibration on a standardised dipole [26], the test antenna with 1 W input power was centred 10 mm distant from the flat section of the phantom without a waterbolus, as shown in Fig. 7.

The simulated and measured SAR patterns are shown in Fig. 8. The peak SAR occurs along the feed diagonal axis with a quasi-symmetric pattern on either side. The simulated and measured peak SAR values are 1.76 and 1.68 W/kg, respectively. Similarly, the simulated and measured iso-50% SAR enclosed areas of 67.25 and 65.25 cm^2, respectively and the iso-25% SAR enclosed areas of 146 and 139 cm^2, respectively. Correspondingly, the discrepancies between simulated and measured peak SAR, iso-50% SAR enclosed area and iso-25% SAR enclosed area are 4.54, 2.97 and 4.79%. The small variances are partially attributed to measurement sensitivities to the antenna–phantom alignment (typically 6% for 0.5 mm position inaccuracy) and phantom dielectric parameter tolerances (typically 5–10%) [25]. Fig. 9 shows the $|S_{11}|$ that accounts for proximity loading by the liquid phantom dielectric. The −8 dB simulated bandwidth of 18.8 MHz (432.3 − 451.0 MHz) compares reasonably to a 29.9 MHz (424.4 − 454.3 MHz) measured bandwidth.

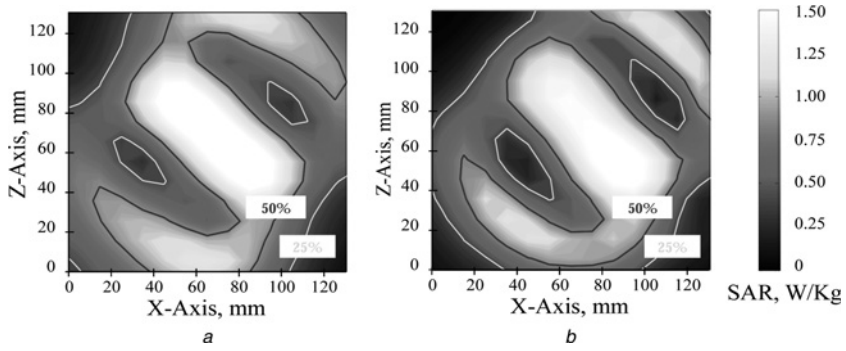

Fig. 8 *SAR distribution*

a Simulated
b Measured

doi: 10.1049/iet-map.2010.0611

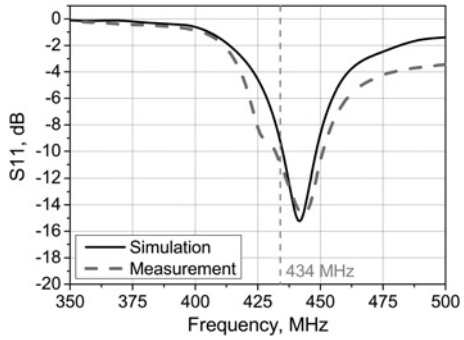

Fig. 9 *$|S_{11}|$ of the antenna at 10 mm from DASY phantom*

5 Discussion

Although comparisons of cubic cell sizes in human body models have indicated that a finer resolution is only necessary for SAR accuracy in tiny organs (e.g. eye lens) [13], the advanced detail in the body model used here reveals some of the additional complexities in the coupling to multiple tissues. A planar tissue model with equivalent tissue layer thicknesses for the epigastrium underestimated the peak SAR by 9.77% compared to the heterogeneous body model.

Comparison of a rectangular waterbolus next to a planar homogeneous muscle and fat-muscle layered models showed that waterbolus thickness is a critical parameter for clinical hyperthermia applications [7, 8]. The optimum thickness of the waterbolus in terms of impedance matching and peak SAR for the three antenna locations has been found to be 6 mm at the antenna radiating axis, but the various body shapes produces different waterbolus thickness (at the antenna periphery) at each body area.

Fig. 10 shows the impedance matching of the antenna at the three body areas with the optimum waterbolus and air-gap combination. The curvature at the back of the head produced the least aperture loading by the tissue. The waterbolus thicknesses at the antenna periphery were 22–34 mm which takes account of possible volume and surface wave oscillations.

The higher peak SAR, which occurred at the head, correlates with an increased tangential *E*-field that typically aligns with the tissue layers. The deepest SAR penetration at the head, inter-scapular and epigastrium locations are located in grey matter, muscle and small intestine, respectively. These tissues have comparable conductivity-to-density ratios.

The SAR has been linked to the permittivity gradient between interfacing tissues [27]. The peak SAR at the

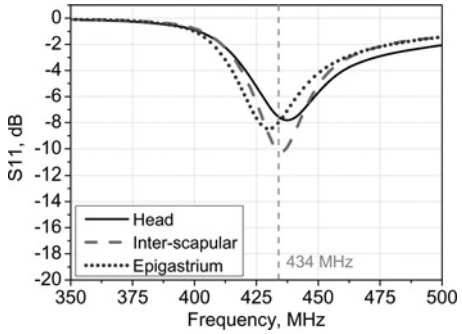

Fig. 10 *$|S_{11}|$ for the optimum waterbolus and air-gap combination for the heterogeneous body model*

Table 3 Input power required for 43°C temperature objective for the heterogeneous body model

Body position	SAR, W/kg	Power for base perfusion rates, W	Power for doubled perfusion rates, W
head	6.41	75	79
inter-scapular	5.28	92	99
epigastrium	6.14	78	81

targeted body areas in the heterogeneous model for the head, inter-scapular and epigastrium positions is 34.4, 28.9 and 35.6% higher than the equivalent homogeneous body models. In general, the SAR penetration is deeper in the homogeneous muscle equivalent models than the heterogeneous tissues. The head position incurred the least power penetration because of the higher absorption rates of the superficial tissues.

The head region presents the highest peak SAR for both the homogeneous muscle and the heterogeneous body models. For the heterogeneous models, the peak SAR is reduced by 4.21% between the head and epigastrium region and by 17.6% between the head and inter-scapular region. For the homogeneous muscle model, the peak SAR is reduced by 5.95% between the head and epigastrium region and 10.7% between the head and inter-scapular region.

The required input power to obtain the 43°C threshold is inversely proportional to the obtained peak SAR at the different body locations. Slight variations are due to the different thermal properties of the tissues at the different locations. The skin and muscle tissues have a perfusion rate that is 76 and 44% higher than fat, respectively. This will require a higher input power to achieve the target temperature of 43°C when tissue perfusion rates are increased for the inter-scapular region, as shown in Table 3.

6 Conclusions

Single-element near-field antenna applicators for superficial hyperthermia treatment require detailed anatomical modelling to take account of the thermal response and should inform on the design performance. A 434 MHz compact patch designed for stable resonance in close proximity to different tissue types and shapes achieves good coupling performance at three areas on a full-body model. The selected source power levels and the energy coupling overcome that natural tissue cooling because of vascular perfusion and perspiration to raise the local temperatures. Notwithstanding the complexity of the anatomy at the various treatment locations, the results indicate that the antenna design features produce a stable energy pattern to target tissue at the centre of the compact applicator geometry.

Contrasted with homogeneous and planar-layered models, the heterogeneous anatomical model reveals how the clinical treatment setup with surface-cooling waterboluses and the patient features influence the SAR patterns. The optimum waterbolus and air-gap dimensions were determined by balancing the impedance matching of the antenna and SAR outcomes. The antenna was modelled at the rear of the head, between the shoulder blades (inter-scapular) and in front of the stomach (epigastrium). The differing surface shapes, sub-dermal features and thermal responses necessitate that different input power levels are selected to achieve equivalent heating effects at the three experimental treatment areas. The input power required to

achieve the target temperature of 43°C was inversely proportional to the peak SAR. The analysis was limited by the static thermal parameters of the model. By doubling the perfusion rates in the tissues, the required input power increased from 75 to 79 W for the head, 92 to 99 W for the inter-scapular and 78 to 81 W for the epigastrium positions. This quantifies the required power levels for clinical treatment scenarios.

7 Acknowledgments

The authors would like to thank TACONIC Advanced Dielectric Division for the antenna materials and Mr. V. Thorne, Dr. H. Tinsley and Dr. J. Murphy for their biomedical guidance. This work was funded by the Irish Research Council for Science, Engineering and Technology's Embark Initiative Postgraduate Scholarship Scheme. It was also supported by Science Foundation Ireland through the CTVR Telecommunications Research Centre and by the Institute for Infocomm Research in Singapore.

8 References

1 Horsman, M.R., Overgaard, J.: 'Hyperthermia: a potent enhancer of radiotherapy', *Clin. Oncol.*, 2007, **19**, (6), pp. 418–426
2 Ichinoseki-Sekine, N., Naito, H., Saga, N., *et al.*: 'Changes in muscle temperature induced by 434 MHz microwave hyperthermia', *Br. J. Sports Med.*, 2007, **41**, (7), pp. 425–429
3 Trujillo, C.J., Leija, L., Vera, A.: 'Design and preliminary evaluation of a superficial applicator for hyperthermia with a new coaxially fed antenna: theoretical models', in 'Pan American Health Care Exchange' (Lima, Peru, 2010), pp. 62–67
4 Samaras, T., Christ, A., Klingenbock, A., Kuster, N.: 'Worst case temperature rise in a one-dimensional tissue model exposed to radiofrequency radiation', *IEEE Trans. Biomed. Eng.*, 2007, **54**, (3), pp. 492–496
5 Bahl, I.J., Stuchly, S.S., Lagendijk, J.W., Stuchly, M.A.: 'Microstrip loop radiators for local hyperthermia'. Proc. IEEE MTT-S Int. Microw. Symp., Los Angeles, CA, USA, June 1981, pp. 465–467
6 Curto, S., Ammann, M.J.: 'Electromagnetic coupling mechanism in a layered human tissue as benchmark for 434 MHz RF hyperthermia applicators'. Proc. IEEE Antennas Propagat. Society Int. Symp., Albuquerque, NM, USA, 2007, pp. 3185–3188
7 Neuman, D.G., Stauffer, P.R., Jacobsen, S., Rossetto, F.: 'SAR pattern perturbations from resonance effects in water bolus layers used with superficial microwave hyperthermia applicators', *Int. J. Hyperth.*, 2002, **18**, (3), pp. 180–193
8 Gelvich, E.A., Mazokhin, V.N.: 'Resonance effects in applicator water boluses and their influence on SAR distribution patterns', *Int. J. Hyperth.*, 2000, **16**, (2), pp. 113–128
9 Lagendijk, J.J.W.: 'Hyperthermia treatment planning', *Phys. Med. Biol.*, 2000, **45**, (1), pp. 61–76
10 Paulides, M.M., Bakker, J.F., Chavannes, N., Van Rhoon, G.C.: 'A patch antenna design for application in a phased-array head and neck hyperthermia applicator', *IEEE Trans. Biomed. Eng.*, 2007, **54**, (11), pp. 2057–2063
11 Curto, S., McEvoy, P., Bao, X.L., Ammann, M.J.: 'Compact patch antenna for electromagnetic interaction with human tissue at 434 MHz', *IEEE Trans. Antennas Propag.*, 2009, **57**, (9), pp. 2564–2571
12 Mason, P.A., Hurt, W.D., Walters, T.J., *et al.*: 'Effects of frequency, permittivity, and voxel size on predicted, specific absorption rate values in biological tissue during electromagnetic-field exposure', *IEEE Trans. Microw. Theory Tech.*, 2000, **48**, (11), pp. 2050–2058
13 Tinniswood, A.D., Furse, C.M., Gandhi, O.P.: 'Power deposition in the head and neck of an anatomically-based human body model for plane wave exposures', *Phys. Med. Biol.*, 1998, **43**, (8), pp. 2361–2378
14 Li, Z., Maccarini, P.F., Arabe, O.A., Stakhursky, V., Joines, W.T., Stauffer, P.R.: 'Towards the validation of a commercial hyperthermia treatment planning system', *Microw. J.*, 2008, **51**, (12), pp. 28–42
15 Ackerman, M.J.: 'The visible human project', *Proc. IEEE*, 1998, **86**, (3), pp. 504–511
16 REMCOM – Electromagnetic Simulation Software, http://www.remcom.com/, accessed December 2010
17 IFAC CNR – Institute for Applied Physics. Italian National Research Council, http://niremf.ifac.cnr.it/tissprop/, accessed December 2010
18 IEEE Std. 1528–2003: 'IEEE Recommended practice for determining the peak spatial-average specific absorption rate (SAR) in the human head from wireless communications devices: measurement techniques', 2003
19 Paulides, M.M., Bakker, J.F., Neufeld, E., *et al.*: 'The HYPERcollar: a novel applicator for hyperthermia in the head and neck', *Int. J. Hyperth.*, 2007, **23**, (7), pp. 567–576
20 Lee, H.K., Antell, A.G., Perez, C.A., *et al.*: 'Superficial hyperthermia and irradiation for recurrent breast carcinoma of the chest wall: prognostic factors in 196 tumors', *Int. J. Rad. Onc. Biol. Phys.*, 1998, **40**, (2), pp. 365–375
21 Van der Zee, J., Vujaskovic, Z., Kondo, M., Sugahara, T.: 'The Kadota fund international forum 2004 – Clinical group consensus', *Int. J. Hyperth.*, 2008, **24**, (2), pp. 111–122
22 Sapareto, S.A., Dewey, W.C.: 'Thermal dose determination in cancer therapy', *Int. J. Radiat. Oncol. Biol. Phys.*, 1984, **10**, (6), pp. 787–800
23 Dewhirst, M.W., Vujaskovic, Z., Jones, E., Thrall, D.: 'Re-setting the biologic rationale for thermal therapy', *Int. J. Hyperth.*, 2005, **21**, (8), pp. 779–790
24 Pennes, H.H.: 'Analysis of tissue and arterial blood temperatures in resting human forearm', *J. Appl. Physiol.*, 1948, **1**, (2), pp. 93–122
25 Schmid and Partner Engineering AG: 'DASY4 dosimetric assessment system manual' (Schmid and Partner Engineering AG, 2002, 1st edn.)
26 Bruijne, M., Samaras, T., Chavannes, N., Rhoon, G.C.: 'Quantitative validation of the 3D SAR profile of hyperthermia applicators using the gamma method', *Phys. Med. Biol.*, 2007, **52**, (11), pp. 3075–3088
27 Gajsek, P., Hurt, W.D., Ziriax, J.M., Mason, P.A.: 'Parametric dependence of SAR on permittivity values in a man model', *IEEE Trans. Biomed. Eng.*, 2001, **48**, (10), pp. 1169–1177

9 Appendix

This section contains Tables 4 and 5 with the conductivity, density, relative permittivity and thermal properties values for the simulated body tissues.

Table 4 Tissue dielectric properties of simulated areas in human body model at 434 MHz

Material	Relative permittivity, ε_r	Conductivity, σ, S/m	Density, ρ, kg/m^3	σ/ρ ratio $\times 10^{-4}$
blood	63.826	1.361	1058	12.9
cancellous bone	22.257	0.241	1920	1.26
cartilage	45.140	0.598	1097	5.45
cortical bone	13.071	0.094	1990	0.47
cerebrospinal fluid	70.630	2.260	1007.2	22.40
grey matter	56.814	0.751	1038	7.24
lung	23.579	0.380	260	14.6
muscle	56.866	0.805	1046.9	7.69
nerve	35.038	0.455	1038	4.39
pancreas	47.120	0.568	1220	4.66
skin	46.059	0.702	1125	6.24
small intestine	65.266	1.922	1042.5	18.4
stomach	67.186	1.013	1050	9.65
white matter	41.659	0.451	1038	4.35
yellow marrow, fat	5.566	0.041	916	0.45

doi: 10.1049/iet-map.2010.0611

Table 5 Tissue thermal properties of simulated areas in human body model at 434 MHz

Material	Heat capacity, C, J/kg/°C	Thermal conductivity, K, W/m/C	Perfusion, ω, ml/100 g/min	Metabolic heat, Q_m, W/m^3
blood	3600	0.51	1000	0
cancellous bone	2238	0.36	3	0
cartilage	3400	0.45	14.3	1000
cortical bone	1300	0.36	1.4	0
cerebrospinal fluid	4200	0.60	0	0
grey matter	3680	0.56	67.1	5370
lung	2354	0.45	40	0
muscle	3500	0.49	5	758
nerve	3640	0.53	56	332.1
pancreas	3600	0.51	100	390.4
skin	3150	0.34	12	1125
small intestine	3600	0.55	100	333.6
stomach	3500	0.52	40	703.5
white matter	3600	0.50	23.7	5370
yellow marrow, fat	2300	0.23	2.8	293.1